

Spatial Autoregressive von-Mises Fisher Regression for Diffusion Tensor Imaging

Zhou Lan

Brigham and Women's Hospital, Harvard Medical School

and

Arkaprava Roy

Department of Biostatistics, University of Florida

November 28, 2022

Abstract

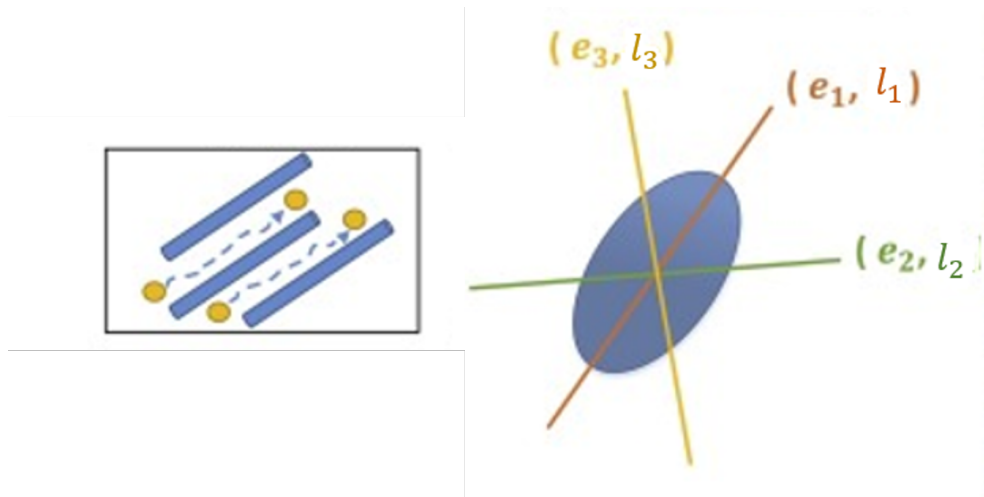
The principal diffusion directions, representing the tissue fiber orientations, are one of the most important markers derived from diffusion tensor imaging (DTI). They are frequently analyzed in several medical studies. However, only a few approaches are available for covariate-dependent statistical analysis for the principal diffusion direction data. To address this gap, we propose a novel generalized linear model to analyze such that using a von Mises Fisher (vMF) distributed error structure. Using a novel link function that relies on the transformation between Cartesian and spherical coordinates, we regress the vMF distributed principal diffusion directions on the subject's covariates. This regression model allows us to measure the importance of the clinical factors on fiber orientations. Furthermore, we impose the spatial dependence to be supported along a given fiber using an autoregressive model. This novel specification renders computational efficiency and flexibility. For Bayesian inference of the directional data, a comprehensive toolbox is thoroughly developed with applications to neuroimaging analysis. We first show the method's empirical efficacy through simulation experiments. Subsequently, applying our regression model to the Alzheimer's Disease Neuroimaging Initiative (ADNI) data, we acquire new insights related to the progression of cognitive impairment.

Keywords: 3 to 6 keywords, that do not appear in the title

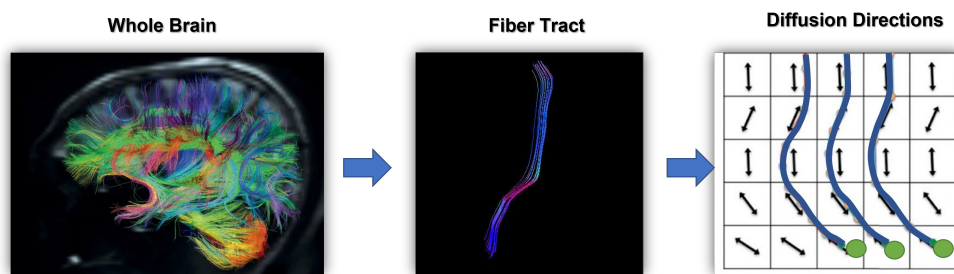
1 Introduction

Neuropathologists routinely investigate the tissue microstructure of the human brain for many neurodegenerative diseases (Reiman and Jagust, 2012; Simmons et al., 1986). There are now several neuroimaging technologies to quantify these features non-invasively. Among those, diffusion tensor imaging (DTI) is widely popular in measuring microstructures with increasing efficiency and accuracy (Soares et al., 2013). This imaging technique measures the diffusivity of water molecules to obtain the voxel-by-voxel white matter tracts. In this imaging technique, an ellipsoid, commonly called a diffusion ellipsoid, represents diffusivity in each voxel (see Figure 1a). Quantitatively, the diffusion ellipsoid is represented by a 3×3 positive definite matrix known as a diffusion tensor. Here, the eigenvectors of the diffusion tensor $[\mathbf{E}_1 \ \mathbf{E}_2 \ \mathbf{E}_3]$ reveals main diffusion directions, and the eigenvalues $[l_1 \ l_2 \ l_3]$ quantify diffusivity along those directions (Zhou, 2010, Section 1.2.3). In summary, the 3×3 diffusion tensor is $[\mathbf{E}_1 \ \mathbf{E}_2 \ \mathbf{E}_3]\text{diag}(l_1, l_2, l_3)[\mathbf{E}_1 \ \mathbf{E}_2 \ \mathbf{E}_3]^T$.

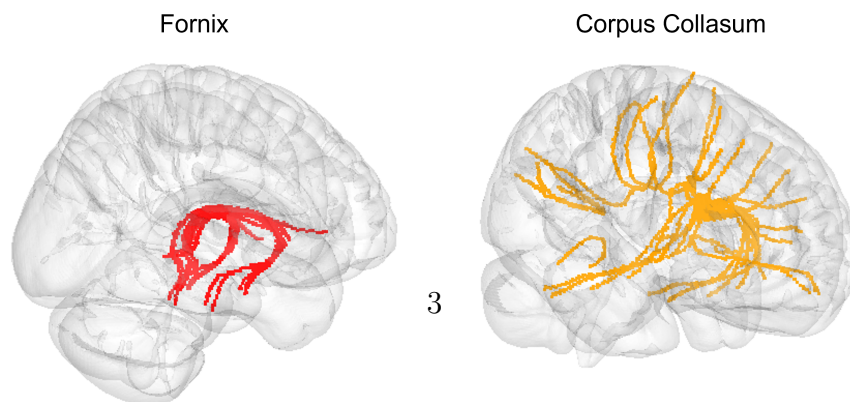
The DTI data has been routinely used for various medical applications. Thus, it has become a popular research area for statisticians to develop novel and useful statistical tools. Several methodological approaches have been introduced in recent years to handle the statistical randomness of the diffusion tensors (Schwartzman, Mascarenhas and Taylor, 2008; Zhu et al., 2009; Yuan et al., 2012; Lee and Schwartzman, 2017; Lan et al., 2021). For example, Schwartzman, Mascarenhas and Taylor (2008) considered a Gaussian distribution for symmetric matrices to model diffusion tensors and developed statistical inference tools for eigenvalues and eigenvectors for this distribution. Following Schwartzman, Mascarenhas and Taylor (2008), Zhu et al. (2009) and Yuan et al. (2012) further introduced intrinsic regression models and polynomial regression models. Adopting matrix-Gamma distribution or Wishart distribution as an alternative random distribution for diffusion tensors, Lee



(a) The left panel provides the tissue to be measured, and the right panel gives the diffusion ellipsoid.



(b) The human brain consists of fibers (left panel). The investigators usually focus on a fiber tract of interest (middle panel). The fiber tract of interest contains the principal eigenvalues of the diffusion tensor in each voxel, and they are interpreted as tangent directions along fiber bundles (right panel).



(c) Tractography atlasThe fornix (left) and corpus callosum (right) are focused in this paper.

Figure 1: The graphical illustrations of the DTI data.

and Schwartzman (2017) provided a inference framework for eigenvalues and eigenvectors. Recently, Lan et al. (2021) proposed a spatial random field based on Wishart distribution to model the diffusion tensors. However, none of these works concerns statistical inferences for the principal eigenvector.

In this work, we focus on the principal eigenvector \mathbf{E}_1 , which is interpreted as the tangent direction along the fiber bundle (Figure 1b). It is thus called the principal diffusion direction in the rest of the paper. It is one of the most important markers for white matter fibers. For example, the principal diffusion directions are often used as an input for tractography algorithms to reconstruct fiber tracts and obtain white matter structural connectivity profiles (Wong et al., 2016). The association between principal diffusion directions and subjects' covariates has been a perspective in studying neurodegenerative disease (Schwartzman, Dougherty and Taylor, 2008). However, the previous works do not consider spatial features of the data, and the statistical tools fail to tackle more complicated clinical problems. Our work aims to study the association between the principal diffusion directions and subject-level covariates (e.g., age, gender, cognitive score, and genetic information) to reveal the factors driving the brain's fiber orientations. To our best knowledge, no methods have been developed to investigate such associations thoroughly.

The principal diffusion directions are directional data (Mardia, 2014). The directional data of dimension p lies on the $(p - 1)$ -dimensional sphere, denoted as \mathcal{S}^{p-1} (Mardia and Jupp, 2009, Section 9.3.2). Given that we focus on the applications to DTI, we set $p = 3$ in the rest of the paper. Due to the manifold nature of this data, it requires unique statistical models for its appropriate characterization. We thus propose our statistical model relying on von Mises–Fisher (vMF) distribution (Mardia, 1975), which is one of the most popular distributions to model statistical randomness in the directional data. Furthermore, our model considers a novel link function that relies on the transformation between Cartesian

and spherical coordinates. This link function allows us to project the principal diffusion direction on the Euclidean space and helps to model the covariate effects efficiently.

Motivated by our neuroimaging applications, the incorporation of spatial dependence is another important component of our work. In the previous works (Wong et al., 2016; Lan et al., 2021), the spatial dependence was based on inter-voxel Euclidean distances. Nevertheless, several studies have raised the need for such characterization for fiber-based analysis. Hence, Goodlett et al. (2009) and Zhu et al. (2011) proposed methods that induce spatial dependence considering arc length distances of a fiber. Currently, these approaches have only been implemented to model the scalar diffusion properties (e.g., fractional anisotropy). In another work, Wong et al. (2007) reported that the diffusion parameters were indeed correlated along the corticospinal tract in healthy individuals. The key step is thus to construct a spatial correlation function supported on the principal diffusion direction space, as discussed in Kang and Li (2016). Therefore, we aim to incorporate such fiber-based dependence. However, one issue is that the fiber tractography is not uniform across all the subjects. Thus, an important feature of our proposed methodology is the integration of the population-averaged fiber tractography information (Yeh et al., 2018) into consideration. Consequently, the spatial variation of the principal diffusion directions is assumed to be autocorrelated along a given fiber defined in this population-averaged fiber tractography. Specifically, our model uses an autoregressive model that induces sequential dependence along the template fiber directions.

Our methodological development is primarily motivated by Alzheimer’s Disease Neuroimaging Initiative (ADNI) study (Mueller et al., 2005). This paper mainly analyzes how the clinical factors affect white matter fiber orientations. Moreover, due to the manifold nature of the data, the traditional posterior summarization methods are unsuitable for the principal diffusion directions. Thus, we develop a novel toolbox for Bayesian angular infer-

ence of principal diffusion direction, addressing the crucial clinical questions of this study. Implementing our novel inference on the ADNI data further reveals several insightful and innovative scientific findings.

To our best knowledge, this is the first paper proposing a spatial generalized regression model for the unit vector-valued responses. The rest of the paper is organized as follows. In Section 2, we provide the details of our motivating data. Driven by the motivating data, our proposed methodology is introduced in Section 3. The proposed Bayesian angular inference scheme is discussed in Section 4. We study the performance of our model in Section 5. Finally, we implement our proposed Bayesian angular inference scheme to infer the ADNI dataset in Section 6. Some concluding remarks are given in Section 7. All the supplementary information are summarized in Supplementary Materials.

2 ADNI Data

Data used in this article were obtained from the ADNI database (adni.loni.usc.edu). ADNI was launched in 2003 as a public-private partnership. The primary goal of ADNI has been to test whether serial magnetic resonance imaging, positron emission tomography, and other biological markers and clinical and neuropsychological assessment can be combined to predict the progression of Alzheimer’s disease. This paper focuses on ADNI-2, which started in September 2011 and continued for five years (Aisen et al., 2010). As stated by the Centers for Disease Control and Prevention (<https://www.cdc.gov/aging/aginginfo/alzheimers.htm>), the symptoms of Alzheimer’s disease are expected to appear after age 60. This motivates us to construct our study cohort targeted at subjects older than 60. The subjects are further categorized into four disease states: healthy controls (CN), early mild cognitive impairment (EMCI), late mild cognitive impairment (LMCI), and Alzheimer’s

Disease (AD). We also collect the subject-level information, including age, gender, minimal state examination (MMSE) score, and Apolipoprotein E (APOE) profile. The MMSE is a performance-based neuropsychological test score, and the score value ranges between 0 and 30; a subject with cognitive impairment is usually associated with a lower MMSE score. The APOE is a genetic marker with three major variants (ϵ -2, ϵ -3, and ϵ -4). Generally, the ϵ -4 variant is the largest known genetic risk factor for Alzheimer’s disease in various ethnic groups (Sadigh-Eteghad et al., 2012). Therefore, in our analysis, we include the variable APOE-4 as a binary indicator standing for the onset of ϵ -4 variant-positive subjects. We also include age and gender in our analysis, as previous studies have established their associations with AD (Podcasy and Epperson, 2022).

The brain fiber tracts associated with cognitive functioning play a crucial role in the progression of AD (Nakata et al., 2008). Among these tracts, fornix and corpus callosum are analyzed in this paper due to their well-established association with cognitive functioning by several previous studies (Oishi et al., 2012; Nowrangi and Rosenberg, 2015; Teipel et al., 2002; Di Paola et al., 2010). The fornix is a C-shaped bundle of nerve fibers in the brain; the corpus callosum is a thick nerve tract consisting of a flat bundle of commissural fibers beneath the cerebral cortex in the brain. The tractography atlases given by Yeh et al. (2018) provide the inter-voxel connectivities along a given fiber tract (see Figure 1c). They are estimated using healthy subjects’ high-quality diffusion-weighted images. We use these tractography atlases (Yeh et al., 2018) for our ADNI data analysis. In the next section, we lay out our proposed model.

3 vMF Regression for Principal Diffusion Directions

We introduce our proposed methodology in this section. In Section 3.1, we first introduce the notations to be used throughout the paper. Section 3.2 describes the vMF distribution used in our regression model for the principal diffusion directions. The link function we use for the regression is illustrated in Section 3.3. Using this link function, we further induce spatial dependence by implementing an autoregressive model in Section 3.4. Section 3.5 provides the prior settings to proceed with our Bayesian inference scheme. Finally, we wrap up with an overall summarization of our model in Section 3.6.

3.1 Notations

For ease of readability, we first define our notations. We let the vector $\mathbf{X}_{gi} = [1, X_{gi1}, \dots, X_{gic}, \dots, X_{giC}]$ to denote the subject-level covariate information of the subject $i \in \{1, 2, \dots, I_g\}$ in the clinical group $g \in \{1, 2, \dots, G\}$ with C -many predictors. Given the tractography atlas, there are K fibers along a given tract (fornix or corpus callosum). Let us further assume that the k -th fiber consists of J_k voxels. We enumerate these voxels as $j = 1, 2, \dots, J_k$ to denote their positioning in the k -th fiber. Any two consecutive indices indicate that the two voxels along that fiber are next to each other. For the i -th subject from the g -th clinical group, we consider \mathbf{E}_{gikj} to denote the principal diffusion direction measured at the j -th voxel on the k -th fiber.

3.2 vMF Distribution

The principal diffusion directions \mathbf{E}_{gikj} are on \mathcal{S}^2 as described before. We assume that the principal diffusion directions \mathbf{E}_{gikj} follow a vMF distribution (Mardia and Jupp, 2009) and

the probability density function is expressed as

$$f\left[\mathbf{E}_{gikj}|\boldsymbol{\mu}_{gikj}, \kappa\right] = C_3(\kappa) \exp\left(\kappa \boldsymbol{\mu}_{gikj}^T \mathbf{E}_{gikj}\right), \quad (1)$$

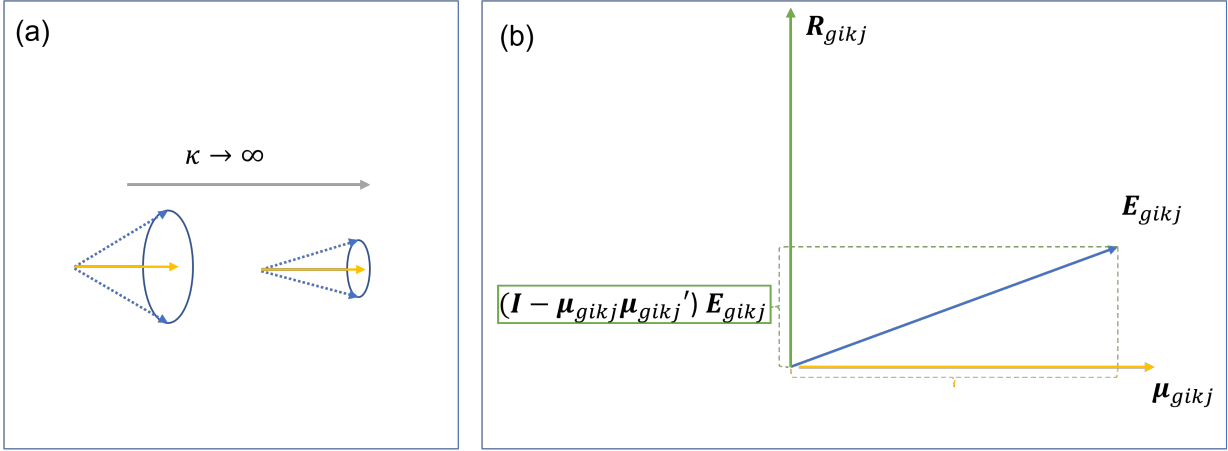
where $C_3(\kappa) = \frac{\kappa}{2\pi(e^\kappa - e^{-\kappa})}$, $\|\boldsymbol{\mu}_{gikj}\| = 1$. In short, we denote it as $\mathbf{E}_{gikj} \sim \text{vMF}(\boldsymbol{\mu}_{gikj}, \kappa)$ and $\|\cdot\|$ stands for the ℓ_2 norm.

In the above density function, the term $\boldsymbol{\mu}_{gikj}^T \mathbf{E}_{gikj}$ can be equivalently represented as $\cos \delta(\boldsymbol{\mu}_{gikj}, \mathbf{E}_{gikj})$ where $\delta(\boldsymbol{\mu}_{gikj}, \mathbf{E}_{gikj})$ is the separation angle between unit vectors $\boldsymbol{\mu}_{gikj}$ and \mathbf{E}_{gikj} . This implies that $\boldsymbol{\mu}_{gikj}$ is the mode direction of this distribution, since setting $\mathbf{E}_{gikj} = \boldsymbol{\mu}_{gikj}$ maximizes the above density with $\delta(\boldsymbol{\mu}_{gikj}, \mathbf{E}_{gikj}) = 0$. Specifically, the density function (Equation 1) is maximized at $\boldsymbol{\mu}_{gikj}$ and minimized at $-\boldsymbol{\mu}_{gikj}$. Furthermore, the parameter κ is called the concentration parameter that controls the concentration of the distribution around the mode direction $\boldsymbol{\mu}_{gikj}$. To be specific, the tangential component $(\mathbf{I} - \boldsymbol{\mu}_{gikj} \boldsymbol{\mu}_{gikj}^T) \mathbf{E}_{gikj}$, lying orthogonal to $\boldsymbol{\mu}_{gikj}$, converges in probability to $\mathbf{0}$ as $\kappa \rightarrow \infty$ (Mardia and Jupp, 2009, Equation 9.3.15) (see Figure 2a).

3.3 Linking to Predictors

Following the generalized linear regression (GLM) framework, we let a linear combination of the predictors be related to the response variables through a link function. It is also reasonable to allow the linear combination of the predictors to be unbounded, as in other GLM frameworks. Therefore, our proposed link function is a convolution of two functions dealing with two layers of transformations. The details of link function construction are provided as follows.

Let (x, y, z) be the Cartesian coordinate of a point on a sphere. Thus, we have $x^2 + y^2 + z^2 = 1$. In spherical coordinate system, it can be represented using two parameters. These two new parameters associated with the spherical coordinate are illustrated in Figure 2b,

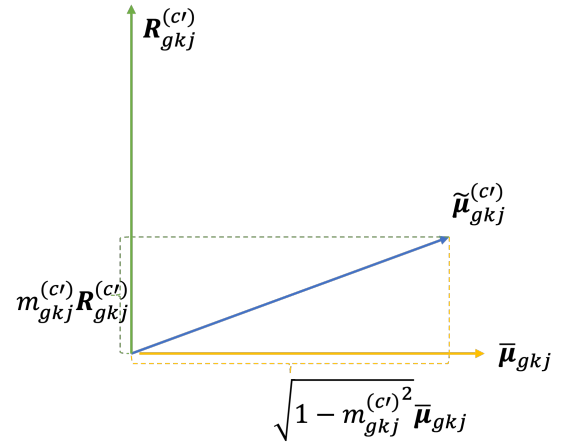


$$(I - \mu_{gikj} \mu_{gikj}') E_{gikj} \xrightarrow{P} \mathbf{0}, \kappa \rightarrow \infty$$

(a) The illustration of concentration parameter κ . In Panel (a), the yellow arrow represents the mode direction μ_{gikj} ; the dashed blue arrows represent the confidence regions \mathcal{C} where $Pr(\mathbf{E}_{gikj} \in \mathcal{C}) = 1 - \alpha$; As $\kappa \rightarrow \infty$, the region \mathcal{C} becomes *narrow*. In Panel (b), the yellow arrow represents the mode direction μ_{gikj} , the blue arrow represents the random vector \mathbf{E}_{gikj} , and the green arrow represents the $\mathbf{R}_{gikj} \in \mathcal{S}^2$. \mathbf{R}_{gikj} and μ_{gikj} are orthogonal to each other. the tangential component $(I - \mu_{gikj} \mu_{gikj}^T) \mathbf{E}_{gikj}$ of \mathbf{E}_{gikj} , a vector describing whether μ_{gikj} is concentrated around the mode direction μ_{gikj} closely.



(b) The graphical illustration describes the transformation between Cartesian and spherical coordinates. The azimuth angle and elevation angle are labeled in the Cartesian coordinate system.



10 (c) The graphical illustration of tangent-normal decomposition of covariate effects. The yellow arrow is the *typical* mode direction; the blue arrow is the *harzard* mode direction; the green arrow is the *deviation* direction; The scalar $m_{gkj}^{(c')} \in (0, 1)$ controls the magnitude of this effect.

Figure 2: The graphical illustrations of directional statistics.

where the azimuth angle $\theta \in [-\pi, \pi]$ is the counterclockwise angle in the x-y plane measured from the positive x-axis and the elevation angle $\phi \in [-\frac{\pi}{2}, \frac{\pi}{2}]$ is the angle with the x-y plane. Then the transformation between Cartesian and spherical coordinates is given by

$$u : (x, y, z) \rightarrow \left(\text{atan2}(y, x), \text{atan2}(z, \sqrt{1 - z^2}) \right) = (\theta, \phi)$$

where $\text{atan2}(y, x) = \lim_{z \rightarrow x^+} (\frac{y}{z}) + \frac{\pi}{2} \text{sgn}(y) \text{sgn}(x) (\text{sgn}(x) - 1)$. Although the spherical coordinates (θ, ϕ) are in Euclidean space, they are bounded. We thus scale the spherical coordinates (θ, ϕ) to the interval $(0, 1)$ and then apply the logit function. Therefore, the map is

$$g : (\theta, \phi) \rightarrow \left(\text{logit}\left(\frac{\theta + \pi}{2\pi}\right), \text{logit}\left(\frac{\phi + \pi/2}{\pi}\right) \right) = (\tilde{\theta}, \tilde{\phi}) \in \mathbb{R} \times \mathbb{R}.$$

Here $\text{logit}(x) = \log\left(\frac{x}{1-x}\right)$ for $0 < x < 1$. This transformation helps us to map our bounded spherical coordinates to a new set of parameters $(\tilde{\theta}, \tilde{\phi})$ that are unbounded. For clarity, we represent the overall mapping from (x, y, z) to $(\tilde{\theta}, \tilde{\phi})$ by $\ell(\cdot)$ which is a convolution of $g(\cdot)$ and $u(\cdot)$, denoted as $\ell(\cdot) := u(\cdot) \circ g(\cdot)$. We use $\ell(x, y, z) = [\tilde{\theta}, \tilde{\phi}]$ to denote this innovative function which projects the directional data in \mathcal{S}^2 to $\mathbb{R} \times \mathbb{R}$.

Our proposed generalized regression model relies on the link function $\ell(\cdot)$. The term $[\tilde{\theta}_{gikj}, \tilde{\phi}_{gikj}]$ is referred to as prediction terms, and it is specified as a function of the covariate vector \mathbf{X}_{gi} , such that $\mathbb{E}[\tilde{\theta}_{gikj}, \tilde{\phi}_{gikj}]^T = [\mathbf{X}_{gi} \boldsymbol{\alpha}_{gkj}, \mathbf{X}_{gi} \boldsymbol{\beta}_{gkj}]^T$. Lemma 1 shows that the link function $\ell(\cdot)$ is a bijective function, and thereby helping us to get a direct mapping between $(\tilde{\theta}_{gikj}, \tilde{\phi}_{gikj})$ and the mode direction $\boldsymbol{\mu}_{gikj}$. In Section 3.4, we lay out our proposed regression model based on this link function.

Lemma 1. *The function $\ell(\cdot) : \mathcal{S}^2 \rightarrow \mathbb{R} \times \mathbb{R}$ is bijective.*

Proof. We know $\ell(\cdot) := u(\cdot) \circ g(\cdot)$ where \circ is function composition. Since $u(\cdot)$ and $g(\cdot)$ are both bijective, $\ell(\cdot)$ is bijective. \square

3.4 Autoregressive Modeling

By preserving $\mathbb{E}[\tilde{\theta}_{gikj}, \tilde{\phi}_{gikj}]^T = [\mathbf{X}_{gi}\boldsymbol{\alpha}_{gkj}, \mathbf{X}_{gi}\boldsymbol{\beta}_{gkj}]^T$, we let $[\tilde{\theta}_{gikj}, \tilde{\phi}_{gikj}]^T = [\mathbf{X}_{gi}\boldsymbol{\alpha}_{gkj} + \epsilon_{gikj}, \mathbf{X}_{gi}\boldsymbol{\beta}_{gkj} + \xi_{gikj}]^T$, where ϵ_{gikj} and ξ_{gikj} are the mean-zero random effects inducing the spatial dependence along the fiber. Incorporation of spatial dependence while analyzing neuroimaging data is crucial for efficient statistical inference. Unlike other neuroimaging applications (Wong et al., 2016; Reich et al., 2018), the key step here is to construct a spatial correlation function supported on a given fiber (Kang and Li, 2016).

The spatial profiling of the DTI statistics indeed reveals that the spatial dependencies depend on the geodesic distances along a fiber, but not on the inter-voxel Euclidean distances (Wong et al., 2007; Goodlett et al., 2009; Zhu et al., 2011). In Section A.1 of the supplementary materials, we visualize $\ell(\mathbf{E}_{gikj})$ of some typical fibers to corroborate this dependence. Following these works, we also incorporate the spatial dependence along a given fiber, as described below. Specifically, the sequential dependencies of principal diffusion directions along a given fiber motivate us to propose the following correlation model relying on an autoregressive characterization for the two error terms ϵ_{gikj} and ξ_{gikj} . We first introduce the definitions and notations related to the Gaussian autoregressive modeling in Definition 2.

Definition 2 (AR- P Process). *Given $A_t = A_{t-1}\Phi_1 + \dots + A_{t-P}\Phi_P + \epsilon_t$ and $\epsilon_t \sim \mathcal{N}(0, \sigma^2)$, for $t \in \mathbb{Z}$. For $t \in \mathbb{Z}$, we define that $\{A_t : t \in \mathbb{Z}\}$ follows a Gaussian AR- P process with correlation parameters (Φ_1, \dots, Φ_P) and variance σ^2 , denoted as $\mathcal{AR}_P([\Phi_1, \dots, \Phi_P], \sigma^2)$.*

We thus have $\{\epsilon_{gikj} : j = 1, 2, \dots, J_k\}$ or $\{\xi_{gikj} : j = 1, 2, \dots, J_k\}$ follow a multivariate normal distribution with an autoregressive covariance matrix, denoted as

$$\begin{aligned} \boldsymbol{\epsilon}_{gik} &= (\epsilon_{gik1}, \dots, \epsilon_{gikj}, \dots, \epsilon_{gikJ_k}) \sim \mathcal{AR}_P([\Phi_{\epsilon 1}, \dots, \Phi_{\epsilon P}], \tau_{\epsilon}^2) \\ \boldsymbol{\xi}_{gik} &= (\xi_{gik1}, \dots, \xi_{gikj}, \dots, \xi_{gikJ_k}) \sim \mathcal{AR}_P([\Phi_{\xi 1}, \dots, \Phi_{\xi P}], \tau_{\xi}^2), \end{aligned} \tag{2}$$

where $(\Phi_{\epsilon,1}, \dots, \Phi_{\epsilon,P}, \tau_\epsilon^2)$ and $(\Phi_{\xi,1}, \dots, \Phi_{\xi,P}, \tau_\xi^2)$ are the corresponding parameters. The above processes are assumed to be independent over $g \in \{1, 2, \dots, G\}$, $i \in \{1, 2, \dots, I_g\}$, and $k \in \{1, 2, \dots, K\}$.

3.5 Prior Settings

We now put priors on the model parameters to proceed with our Bayesian inference. For the regression coefficients, we assign AR- P process priors, denoted as

$$\begin{aligned}\boldsymbol{\alpha}_{gk}(c) &= \left(\alpha_{gk1}(c), \dots, \alpha_{gkj}(c), \dots, \alpha_{gkJ_k}(c) \right) \sim \mathcal{AR}_P \left([\Phi_{\alpha,1}, \dots, \Phi_{\alpha,P}], \sigma_\alpha^2 \right) \\ \boldsymbol{\beta}_{gk}(c) &= \left(\beta_{gk1}(c), \dots, \beta_{gkj}(c), \dots, \beta_{gkJ_k}(c) \right) \sim \mathcal{AR}_P \left([\Phi_{\beta,1}, \dots, \Phi_{\beta,P}], \sigma_\beta^2 \right),\end{aligned}\tag{3}$$

where $\boldsymbol{\alpha}_{gkj} = \left(\alpha_{gkj}(0), \dots, \alpha_{gkj}(c), \dots, \alpha_{gkj}(C) \right)$ and $\boldsymbol{\beta}_{gkj} = \left(\beta_{gkj}(0), \dots, \beta_{gkj}(c), \dots, \beta_{gkj}(C) \right)$. The terms $\alpha_{gkj}(0)$ and $\beta_{gkj}(0)$ are the coefficients for the intercepts. The terms $\alpha_{gkj}(c)$ and $\beta_{gkj}(c)$ are the coefficients for the covariate c . The variances are assigned with weakly informative inverse-gamma priors with shape and rate parameters set to 0.1, denoted as $\tau_\epsilon^{-2}, \tau_\xi^{-2}, \sigma_\alpha^{-2}, \sigma_\beta^{-2} \sim \mathcal{GA}(0.1, 0.1)$. We put a diffuse prior for the concentration parameter, κ , denoted as $\kappa \propto 1$. The concentration parameter κ can be viewed as a nugget effect. An autoregressive process with the partial autocorrelation parameters restricted to $(-1, 1)$ can ensure stationarity (Barnett et al., 1996). Therefore, we assign uniform $(-1, 1)$ prior on the partial autocorrelation parameters. Specifically, $\rho_{\alpha,p}, \rho_{\beta,p}, \rho_{\epsilon,p}, \rho_{\xi,p} \sim \mathcal{U}(-1, 1)$ for $p \in \{1, 2, \dots, P\}$, where $\rho_{\alpha,p}, \rho_{\beta,p}, \rho_{\epsilon,p}, \rho_{\xi,p}$ are the corresponding partial autocorrelation parameters associated with the autoregressive process priors for $\boldsymbol{\alpha}_{gk}(c)$'s, $\boldsymbol{\beta}_{gk}(c)$'s, and the autoregressive random effects $\boldsymbol{\epsilon}_{gik}$'s, and $\boldsymbol{\xi}_{gik}$'s, respectively. Applying the Durbin-Levinson recursion on the partial autocorrelations $(\rho_{\alpha,p}, \rho_{\beta,p}, \rho_{\epsilon,p}, \rho_{\xi,p})$, we get back the autoregressive coefficients $(\Phi_{\alpha,p}, \Phi_{\beta,p}, \Phi_{\epsilon,p}, \Phi_{\xi,p})$ using the R functions `inla.ar.pacf2phi()` and the

reverse transformation is applied using `inla.ar.phi2pacf()` from the R package `inla` (Lindgren and Rue, 2015).

3.6 Model Summary

By breaking the above model construction into three generic stages, i.e., data model, process model, and prior model, we summarize our proposed spatial vMF regression model for principal diffusion directions below.

Data Model:

For $g \in \{1, 2, \dots, G\}$, $i \in \{1, 2, \dots, I_g\}$, $k \in \{1, 2, \dots, K\}$, and $j \in \{1, 2, \dots, J_k\}$

$$f\left[\mathbf{E}_{gikj} | \boldsymbol{\mu}_{gikj}, \kappa\right] = C_3(\kappa) \exp\left(\kappa \boldsymbol{\mu}_{gikj}^T \mathbf{E}_{gikj}\right), \quad C_3(\kappa) = \frac{\kappa}{2\pi(e^\kappa - e^{-\kappa})} \quad \|\boldsymbol{\mu}_{gikj}\| = 1,$$

$$\ell\left(\boldsymbol{\mu}_{gikj}\right) = [\tilde{\theta}_{gikj}, \tilde{\phi}_{gikj}]^T = [\mathbf{X}_{gi} \boldsymbol{\alpha}_{gkj} + \epsilon_{gikj}, \mathbf{X}_{gi} \boldsymbol{\beta}_{gkj} + \xi_{gikj}]^T,$$

$$\boldsymbol{\alpha}_{gkj} = \left(\alpha_{gkj}(0), \dots, \alpha_{gkj}(c), \dots, \alpha_{gkj}(C)\right),$$

$$\boldsymbol{\beta}_{gkj} = \left(\beta_{gkj}(0), \dots, \beta_{gkj}(c), \dots, \beta_{gkj}(C)\right),$$

Process Model:

for $g \in \{1, 2, \dots, G\}$, $i \in \{1, 2, \dots, I_g\}$, $k \in \{1, 2, \dots, K\}$

$$\boldsymbol{\epsilon}_{gik} = (\epsilon_{gik1}, \dots, \epsilon_{gikj}, \dots, \epsilon_{gikJ_k}) \sim \mathcal{AR}_P\left([\Phi_{\epsilon 1}, \dots, \Phi_{\epsilon P}], \tau_\epsilon^2\right), \quad (4)$$

$$\boldsymbol{\xi}_{gik} = (\xi_{gik1}, \dots, \xi_{gikj}, \dots, \xi_{gikJ_k}) \sim \mathcal{AR}_P\left([\Phi_{\xi 1}, \dots, \Phi_{\xi P}], \tau_\xi^2\right),$$

Prior Model:

$$\tau_\epsilon^{-2}, \tau_\xi^{-2}, \sigma_\alpha^{-2}, \sigma_\beta^{-2} \sim \mathcal{GA}(0.1, 0.1)$$

For $g \in \{1, 2, \dots, G\}$, $k \in \{1, 2, \dots, K\}$, $c \in \{0, 1, 2, \dots, C\}$

$$\boldsymbol{\alpha}_{gk}(c) = \left(\alpha_{gk1}(c), \dots, \alpha_{gkj}(c), \dots, \alpha_{gkJ_k}(c)\right) \sim \mathcal{AR}_P\left([\Phi_{\alpha, 1}, \dots, \Phi_{\alpha, P}], \sigma_\alpha^2\right),$$

$$\boldsymbol{\beta}_{gk}(c) = \left(\beta_{gk1}(c), \dots, \beta_{gkj}(c), \dots, \beta_{gkJ_k}(c)\right) \sim \mathcal{AR}_P\left([\Phi_{\beta, 1}, \dots, \Phi_{\beta, P}], \sigma_\beta^2\right),$$

For $p \in \{1, 2, \dots, P\}$

$$\rho_{\alpha, p}, \rho_{\beta, p}, \rho_{\epsilon, p}, \rho_{\xi, p} \sim \mathcal{U}(-1, 1).$$

We use the Markov chain Monte Carlo (MCMC) algorithm to generate the posterior samples for our Bayesian inference. The MCMC scheme consists of Metropolis-Hastings-within-Gibbs steps. For all the numerical studies presented in the following sections, we collect 3,000 MCMC samples after discarding the first 2,000. The source codes for im-

plementation are attached in Section B.1 of the supplementary materials. To maintain computational simplicity, we keep the same order for all the AR processes both in the spatial random effects (ξ_{gik} 's and ϵ_{gik} 's) and the priors for the coefficients ($\alpha_{gk}(c)$'s and $\beta_{gk}(c)$'s). Since accurate lag estimation is not our primary interest, the above simplification would not affect our inference. In Section 4, we introduce a novel Bayesian angular inference framework for making inferences on the principal diffusion direction data. This novel Bayesian inference framework can be used to tackle the important scientific questions related to our ADNI study.

4 Bayesian Angular Inference for Principal Diffusion Directions

This section introduces our novel Bayesian angular inference for principal diffusion directions. The proposed inference framework not only tackles the critical scientific questions related to DTI analysis but also enriches the toolbox for statistical inference of directional data. In Section 4.1, we introduce a novel angular expectation, which provides us with a more appropriate metric for inferring directional statistics. Based on this convenient tool, we further propose the strategies for the characterization of covariate effects (Section 4.2) and the regions of differences (Section 4.3).

4.1 Angular Expectation

For a random unit vector $\boldsymbol{\mu}$, the angular expectation is defined as

$$\mathbb{A}\boldsymbol{\mu} = \arg \min_{\boldsymbol{m} \in \mathcal{S}^2} \int \delta(\boldsymbol{m}, \boldsymbol{\mu}) \pi(\boldsymbol{\mu}) d\boldsymbol{\mu},$$

where \mathbb{A} is introduced as an operator returning the angular expectation, p is the dimension of $\boldsymbol{\mu}$, and $\pi(\boldsymbol{\mu})$ stands for the distribution of $\boldsymbol{\mu}$. The angular expectation \mathbb{A} is the main tool for our proposed Bayesian angular inference scheme. For a new subject in group g with the covariate vector $\mathbf{X}_{g,\text{new}}$, the posterior predictive distribution of the mode direction $\boldsymbol{\mu}_{g,\text{new},kj}$ for the j -th voxel on the k -th fiber based on (4), is $\left[\boldsymbol{\mu}_{g,\text{new},kj}|\mathbf{X}_{g,\text{new}};\text{data}\right]$. For clarity, we use subscript “new” to replace the original subscript “ i ” in the model for referring to a new subject.

For summarizing above posterior of $\boldsymbol{\mu}_{g,\text{new},kj}$, we compute the posterior angular expectation using the MCMC samples $\{\boldsymbol{\mu}_{g,\text{new},kj}^{(t)} : t = 1 : T\}$ as

$$\mathbb{A}\left[\boldsymbol{\mu}_{g,\text{new},kj}|\mathbf{X}_{g,\text{new}};\text{data}\right] \approx \arg \min_{\mathbf{m} \in \mathcal{S}^2} \frac{1}{T} \sum_{t=1}^T \delta(\mathbf{m}, \boldsymbol{\mu}_{g,\text{new},kj}^{(t)}) = \frac{\sum_{t=1}^T \boldsymbol{\mu}_{g,\text{new},kj}^{(t)}/T}{\left\| \sum_{t=1}^T \boldsymbol{\mu}_{g,\text{new},kj}^{(t)}/T \right\|}.$$

Relating to our ADNI data analysis, the angular expectation $\mathbb{A}\left[\boldsymbol{\mu}_{g,\text{new},kj}|\mathbf{X}_{g,\text{new}};\text{data}\right]$ for $k = 1 : K$ and $j = 1 : J_k$ profiles the expected fiber direction after the model-based adjustment for the covariate vector $\mathbf{X}_{g,\text{new}}$.

4.2 Tangent-Normal Decomposition to Investigate Covariate Effects

A transparent inference framework illustrating the covariate effects is essential for clinical studies. In our proposed model, the coefficients $\boldsymbol{\alpha}_{gkj}$ and $\boldsymbol{\beta}_{gkj}$ do not offer a straightforward illustration of the covariate effects on the mode directions. Therefore, we incorporate the tangent-normal decomposition (Mardia and Jupp, 2009, Page 169) to summarize the covariate effects on principal diffusion direction as follows.

4.2.1 Step 1: Specification of *Typical* Covariate Vector and *Hazard* Covariate Vector

Let the effect of covariate c' in the g -th group is of interest. Our proposed procedure starts by defining the following two covariate vectors: a) \mathbf{X}_{gT} : Covariate vector of a subject in the *typical* clinical condition of the g -th clinical group; b) $\mathbf{X}_{gH}^{(c')}$: Covariate vector of a subject in the *hazard* clinical condition of the g -th clinical group. Thus, we replace the original subscript “ i ” with “T” and “H” in our notation, to represent a subject in the *typical* and *hazard* condition, respectively.

A subject under the *typical* clinical condition in the g -th clinical group is a subject with the covariate vector \mathbf{X}_{gT} , being set as $\mathbf{X}_{gT} = [1, X_{gT1}, \dots, X_{gTc}, \dots, X_{gTC}]$. If the covariate is continuous (e.g., age, MMSE score), the term X_{gTc} is specified as its sample mean over all subjects within the g -th clinical group in the data, i.e., $X_{gTc} = \frac{1}{I_g} \sum_{i=1}^{I_g} X_{gic}$. In the case of binary (0/1) predictors (gender and APOE-4), the term X_{gTc} is set based on a pre-specified baseline. In this analysis, we consider a subject without ϵ -4 variant as baseline, i.e., $X_{gT, \text{APOE-4}} = 0$. For studying the effect of gender, a similar strategy can be adopted. However, our current analysis is carried out for the two genders separately. Note that the specification of the *typical* covariate vector is group-specific, and it is not subject to change with the covariate of interest.

A general assumption for a subject under the *hazard* clinical condition from the g -th clinical group is that the subject is at risk when compared to the *typical* clinical condition. We refer to a *hazard* subject’s covariate as $\mathbf{X}_{gH}^{(c')}$ when the effect of c' is of interest. To investigate the effect of one covariate, we specify the *hazard* covariate vector as $\mathbf{X}_{gH}^{(c')} = [1, X_{gT1}, \dots, X_{gHc'}, \dots, X_{gTC}]$. Except for covariate c' , all the other covariates are set to the same values as in the *typical* covariate vector. If c' is a continuous predictor (e.g., age, MMSE score), the term $X_{gHc'}$ is set based on the study design. In our study, when c' stands

for age, the term $X_{gHc'}$ is set as $X_{gHc'} = X_{gTc'} + 1$, thereby allowing us to quantify the possible effect of increment in age. If the covariate c' is the MMSE score, the term $X_{gHc'}$ is set as $X_{gHc'} = X_{gTc'} - 1$ which allows us to investigate the effect of the decrease in MMSE score. If the covariate is a binary (0/1) predictor, the term $X_{gHc'}$ is specified according to the pre-specified baseline. In our analysis, if the covariate is APOE-4, we set $X_{gHc'} = 1$ to make the *hazard* condition as the subject with ϵ -4 variant. This helps us to understand the covariate effect if a subject has ϵ -4 variant.

4.2.2 Step 2: Computation of *Typical* Mode Directions and *Hazard* Mode Directions

Next, we obtain the corresponding predictive posterior distributions of the mode directions with the given *typical* or *hazard* covariate vector. They are referred as to the *typical* and *hazard* mode direction, respectively, expressed as follows: a) *Typical* Mode Direction: $\bar{\boldsymbol{\mu}}_{gkj} := [\boldsymbol{\mu}_{gTkj} | \mathbf{X}_{gT}; \text{data}]$; b) *Hazard* Mode Direction: $\tilde{\boldsymbol{\mu}}_{gkj}^{(c')} := [\boldsymbol{\mu}_{gHkj} | \mathbf{X}_{gH}^{(c')}; \text{data}]$. They can also be approximately learned from the MCMC outputs.

4.2.3 Step 3: Decompose the Hazard Mode Direction along the Typical Mode Direction

To quantify the covariate effect, we employ the tangent-normal decomposition on the *hazard* mode direction $\tilde{\boldsymbol{\mu}}_{gkj}^{(c')}$ as in Figure 2c where the *typical* mode direction $\bar{\boldsymbol{\mu}}_{gkj}$ is the tangent direction and the term $\mathbf{R}_{gkj}^{(c')}$ is the normal direction. Applying this to the principal diffusion directions, the term $\mathbf{R}_{gkj}^{(c')}$ can be interpreted as the *deviation* direction that the covariate c' exerts, conditioning on other covariates. The scalar $m_{gkj}^{(c')} \in (0, 1)$, which controls the magnitude of this effect, can be used to quantify the importance of this covariate: the larger value of $m_{gkj}^{(c')}$ indicates the stronger effect of covariate c' . Computationally, the

tangent-normal decomposition can be applied to each MCMC sample t . This provides us with the posterior samples of $\mathbf{R}_{gkj}^{(c')}$ and $m_{gkj}^{(c')}$, denoted as $\{\mathbf{R}_{gkj}^{(c')}(t) : t = 1 : T\}$ and $\{m_{gkj}^{(c')}(t) : t = 1 : T\}$. We use those samples to obtain posterior estimates of $\mathbb{A}[\mathbf{R}_{gkj}^{(c')}|\text{data}]$ to spatially profile the *deviation* directions caused by the covariate c' . Similarly, the posterior mean estimate of $m_{gkj}^{(c')}$ can also be computed and used to quantify the magnitude of the covariate effect.

4.3 Regions of Differences Characterized by Separation Angle

Especially in neuroimaging analysis, characterizing regions of differences across the different clinical groups are often of great interest. We propose a novel separation angle-based method for principal diffusion directions to characterize regions of differences. For each clinical group g , we get the angular expected mean for all voxels of a subject i as $\mathbb{A}[\boldsymbol{\mu}_{gikj}|\mathbf{X}_{gikj}; \text{data}]$. Subsequently, we get the *sample* angular mean over the subjects in the g -th group, as $\hat{\boldsymbol{\mu}}_{gkj} = \arg \min_{\mathbf{m} \in \mathcal{S}^2} \sum_{i=1}^{I_g} \delta(\mathbf{m}, \mathbb{A}[\boldsymbol{\mu}_{gikj}|\mathbf{X}_{gikj}; \text{data}])$. Finally, the regions of differences between any two groups can be characterized by the separation angle defined as $\Delta_{g,g'}(v) = \delta(\hat{\boldsymbol{\mu}}_{gkj}, \hat{\boldsymbol{\mu}}_{g'kj})$. The values of $\Delta_{g,g'}(v)$ can be used to illustrate the regions of differences between any two clinical groups. Applying this to our ADNI data, we are able to quantify the group differences among different disease groups in Section 6.2.

5 Model Comparison

In this section, we conduct numerical studies on the ADNI and synthetic principal diffusion direction data to demonstrate the performance of our proposed vMF regression compared to other traditional alternatives. The primary assumption of our proposal is that the principal diffusion directions are the realizations of a vMF distribution as $\mathbf{E}_{gikj} \sim \text{vMF}(\boldsymbol{\mu}_{gikj}, \kappa)$.

This assumption guarantees that $\mathbf{E}_{gikj} \in \mathcal{S}^2$. However, there is a limiting equivalence between vMF distribution and multivariate Gaussian for large κ as presented in Lemma 3 (Song and Dunson, 2022, Lemma 1).

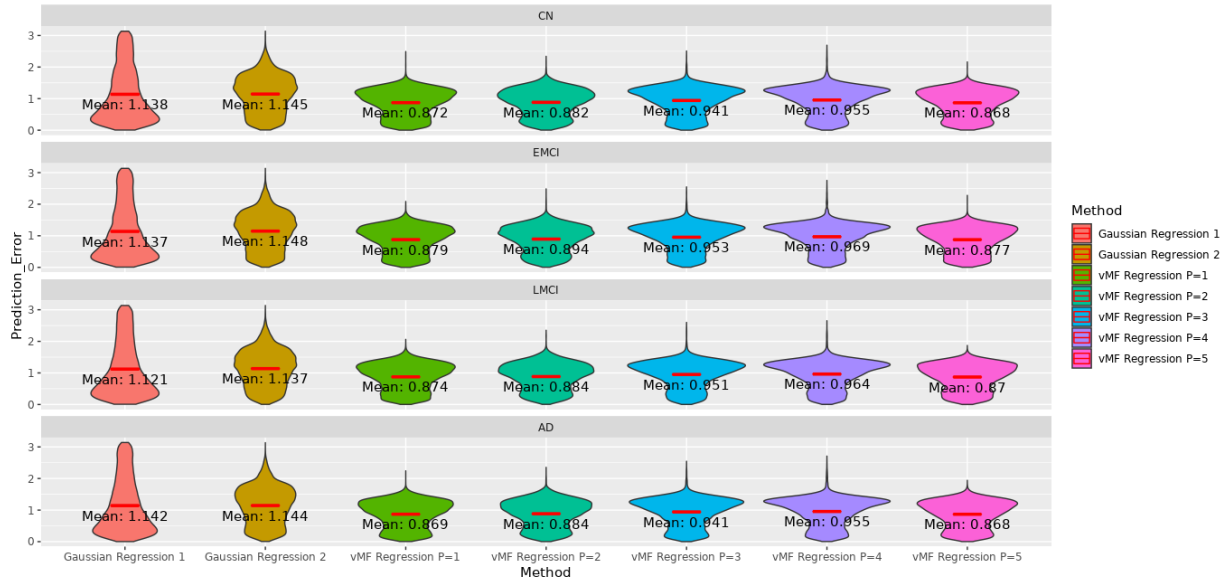
Lemma 3. *If $\mathbf{E} \sim vMF(\boldsymbol{\mu}, \kappa)$, as $\kappa \rightarrow \infty$, then $\sqrt{\kappa}[\mathbf{E} - \boldsymbol{\mu}] \rightarrow \mathcal{N}(\mathbf{0}, (\mathbf{I} - \boldsymbol{\mu}\boldsymbol{\mu}^T))$ and $\sqrt{\kappa}[\ell(\mathbf{E}) - \ell(\boldsymbol{\mu})] \rightarrow \mathcal{N}(\mathbf{0}, \nabla\ell(\boldsymbol{\mu})^T(\mathbf{I} - \boldsymbol{\mu}\boldsymbol{\mu}^T)\nabla\ell(\boldsymbol{\mu}))$, where $\nabla\ell(\boldsymbol{\mu})$ is the gradient of $\ell(\boldsymbol{\mu})$ with respect of $\boldsymbol{\mu}$.*

Hence, we consider two competing methods based on multivariate Gaussian distribution: 1) *Gaussian Regression 1*: a multivariate regression model for the principal diffusion directions \mathbf{E}_{gikj} , 2) *Gaussian Regression 2*: a multivariate regression model for transformed means $\ell(\mathbf{E}_{gikj})$. Specific details are described as follows. The *Gaussian Regression 1* simply treats the principal diffusion directions \mathbf{E}_{gikj} as normally distributed random variables, such that $\mathbf{E}_{gikj} \sim \mathcal{N}(\boldsymbol{\mu}_{gikj}, \boldsymbol{\Sigma}_1)$, where $\boldsymbol{\mu}_{gikj}^{(p)} = \mathbf{X}_{gi}\mathbf{u}_{gkj}^{(p)}$, $\boldsymbol{\mu}_{gikj}^{(p)}$ is the p -th element of $\boldsymbol{\mu}_{gikj}$ for $p \in \{1, 2, 3\}$, i.e., $\boldsymbol{\mu}_{gikj} = (\boldsymbol{\mu}_{gikj}^{(1)}, \boldsymbol{\mu}_{gikj}^{(2)}, \boldsymbol{\mu}_{gikj}^{(3)})$. Alternatively, in case of *Gaussian Regression 2*:, the terms $\ell(\mathbf{E}_{gikj}) = [A_{gikj}, B_{gikj}]^T$ are assumed to follow a normal distribution, denoted as $\ell(\mathbf{E}_{gikj}) = [A_{gikj}, B_{gikj}]^T \sim \mathcal{N}([\tilde{\boldsymbol{\theta}}_{gikj}, \tilde{\boldsymbol{\phi}}_{gikj}]^T, \boldsymbol{\Sigma}_2)$, where $\tilde{\boldsymbol{\theta}}_{gikj} = \mathbf{X}_{gi}\mathbf{a}_{gkj}$ and $\tilde{\boldsymbol{\phi}}_{gikj} = \mathbf{X}_{gi}\mathbf{b}_{gkj}$. We take the Bayesian route for inference for all these methods and put weakly informative priors on the unknown parameters. Specifically, we give normal priors with mean $\mathbf{0}$ and covariance matrix $1000 \times \mathbf{I}$ on the coefficients, denoted as $\mathbf{u}_{gkj}^{(1)}, \mathbf{u}_{gkj}^{(2)}, \mathbf{u}_{gkj}^{(3)}, \mathbf{a}_{gkj}, \mathbf{b}_{gkj} \sim \mathcal{N}(\mathbf{0}, 1000 \times \mathbf{I})$. We further put inverse Wishart prior with degrees of freedom 5 and scale matrix \mathbf{I} on the covariance matrices, denoted as $\boldsymbol{\Sigma}_1^{-1}, \boldsymbol{\Sigma}_2^{-1} \sim \mathcal{W}(5, \mathbf{I})$. Our inference is based on the MCMC algorithm, where we collect 3,000 post-burn samples after discarding the first 2,000. The MCMC convergence is monitored by Heidelberger and Welch's convergence diagnostic (Heidelberger and Welch, 1981).

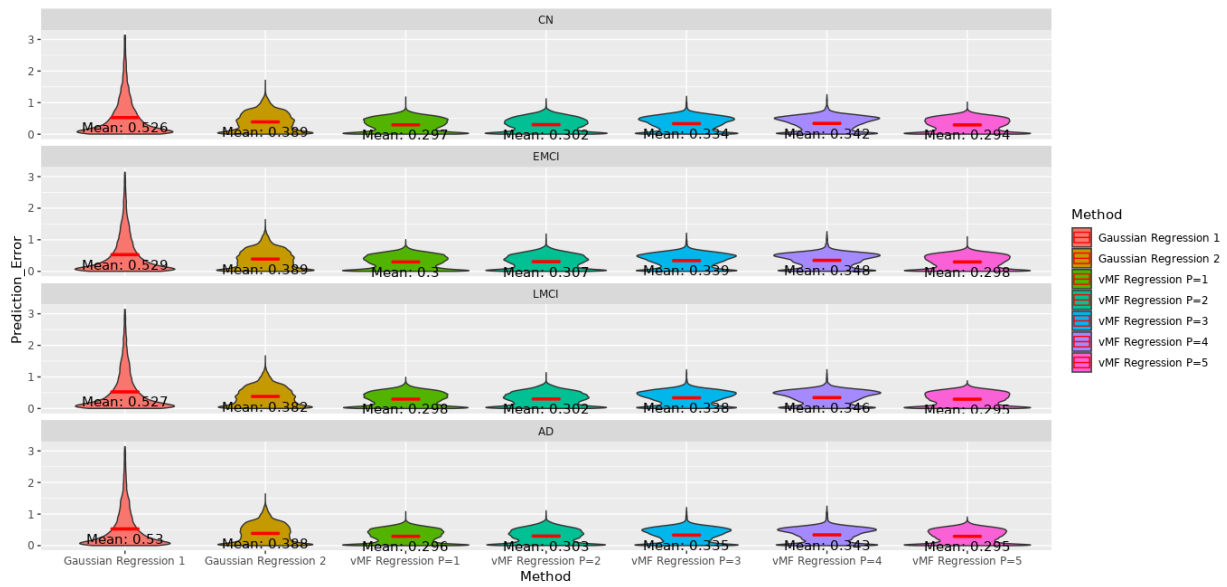
First, we apply the models to the motivating ADNI data. We randomly divide the data 50/50 into training and validation sets. The training data is used to fit the model first and get the parameter estimates. Based on that, we obtain the predictive posterior *estimate* of $\boldsymbol{\mu}_{gikj}$ with the covariate vector of the validation data. As described in Section 2, the covariate vector includes the intercept, age, gender, MMSE score, and APOE-4 information. We use $\widehat{\boldsymbol{\mu}}_{gikj}$ to denote this *estimate*, and the different methods obtain this *estimate* in different ways. For *Gaussian Regression 1*, we compute the posterior estimate of $\boldsymbol{\mu}_{gikj}$ directly by averaging the posterior samples. For *Gaussian Regression 2* and our proposed vMF regression, we use the angular expectation as introduced in Section 4. Specifically, for the vMF regression, we set the number of lags $P \in \{1, \dots, 5\}$. Subsequently, we compute their corresponding prediction errors on the validation data for comparison. The prediction errors are quantified in terms of the separation angle $\delta(\widehat{\boldsymbol{\mu}}_{gikj}, \mathbf{E}_{gikj})$ and the root mean squared error $\|\widehat{\boldsymbol{\mu}}_{gikj} - \mathbf{E}_{gikj}\|$.

In Figure 3 and 4, we show the prediction errors associated with the fornix and corpus callosum, respectively. Our proposed method performs overwhelmingly better than the alternatives based on average errors. The prediction performance of the vMF regression is the best among all the competing methods considered here. Moreover, from the results of the motivating data only, any choice of the lag $P \in \{1, \dots, 5\}$ leads to better performance than the two alternatives.

Next, we generate synthetic principal diffusion direction data following our proposed vMF regression model. Similar to the ANDI data, we decompose the synthetic data into training and validation data. In both of the training data and the validation data, we set the sample size of each clinical group as $N_g = 20$ with a total of $G = 4$ clinical groups. Hence, the total sample size of each group is 40. We create a synthetic fiber tract which contains $K = 12$ fibers and 1,256 voxels in total. For each data replication, the same sets

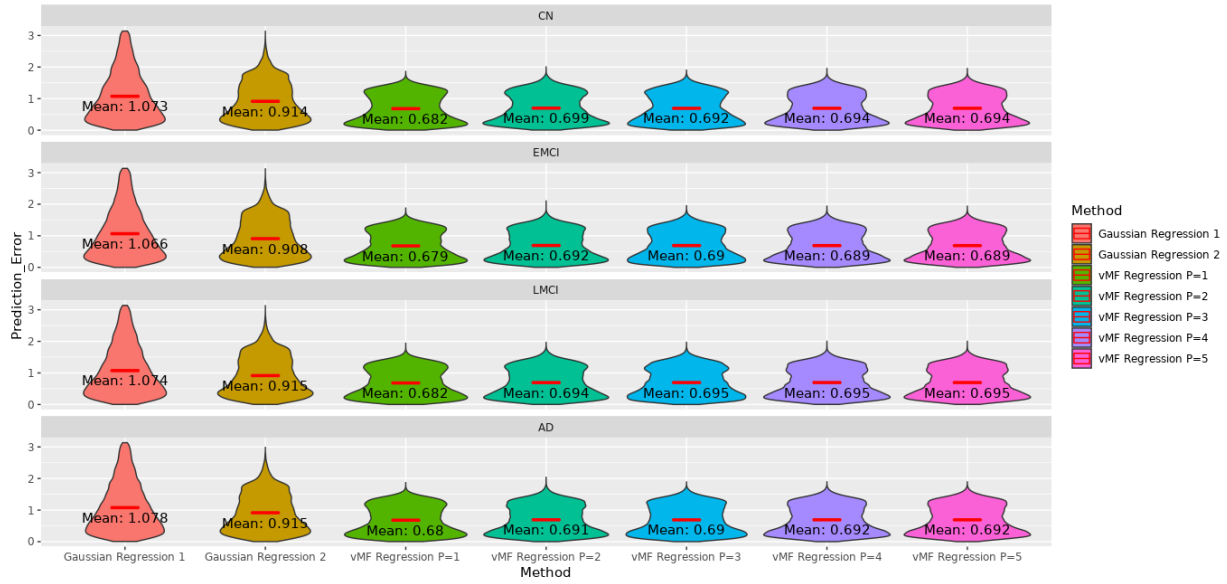


(a) Angular Separation

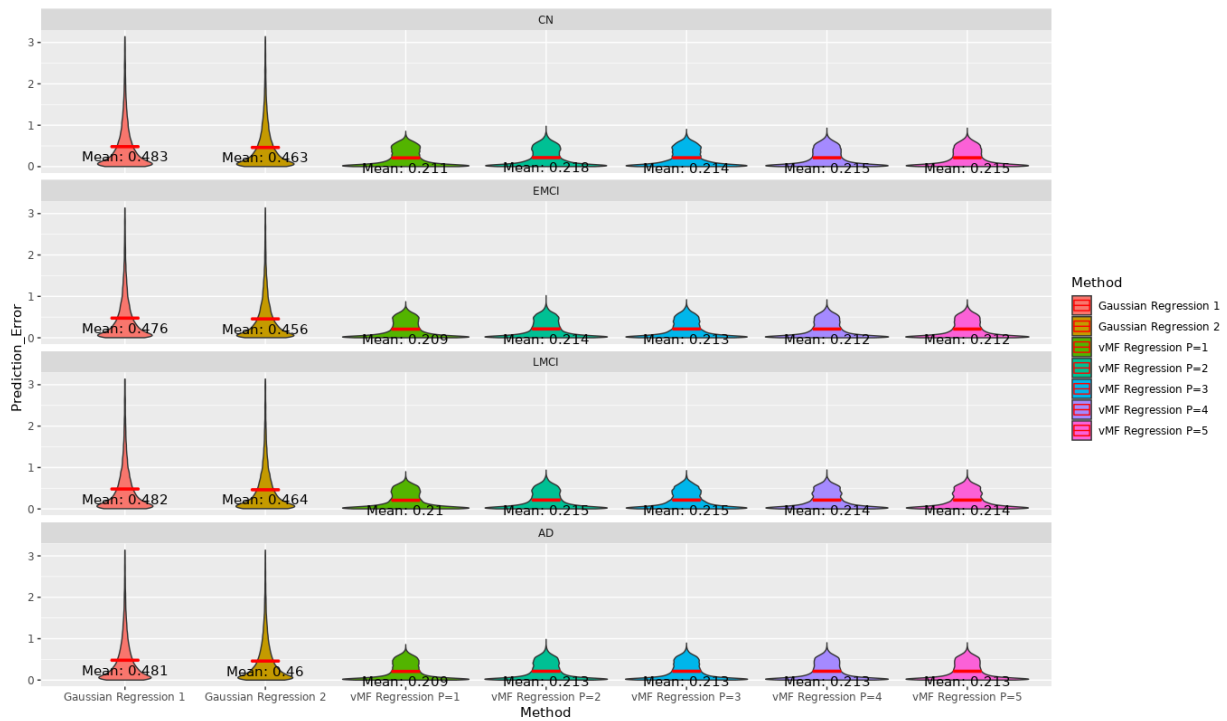


(b) Root Square Error

Figure 3: Prediction error within fornix: The violin plots show the prediction error of methods. The x-axis is for methods, and the y-axis is for prediction error. The panel (a) is based on the angular separation; the panel (b) is based on the root square error.



(a) Separation Angle



(b) Root Mean Squared Error

Figure 4: Prediction error within corpus callosum: The violin plots show the prediction error of methods. The x-axis is for methods, and the y-axis is for prediction error. The panel (a) is based on the angular separation; the panel (b) is based on the root square error.

of tractography atlas, covariate vectors, and voxel-wise coefficients are used that are stored in the R file `synthetic.Rdata` attached in Section B.2 of the supplementary materials. We set $P = 5$ and generate the partial correlation coefficients from $\mathcal{U}(-1, 1)$. The variances are set as $\tau_\epsilon^2 = \tau_\xi^2 = \sigma_\alpha^2 = \sigma_\beta^2 = 1$. For each replication, we also consider multiple choices for the concentration parameter as $\kappa \in \{10, 30, 50\}$ to validate Lemma 3 that the vMF distribution and the Gaussian distribution become equivalent when κ is sufficiently large. Our final results are based on 50 replicated data-sets in total for each setting. Furthermore, for the vMF regression, we compare the results for the lags $P \in \{1, \dots, 9\}$.

We illustrate the prediction errors over all the subjects, voxels, and replications in Section A.2 of the supplementary materials. Similar to the real data results, our proposed method again registers an overwhelmingly better performance than the Gaussian alternatives. We also find that larger κ produces better results for the Gaussian distribution-based methods. This is an expected result due to Lemma 3. Furthermore, the vMF regression with $P = 5$ performs relatively better among $P \in \{1, \dots, 9\}$ while the data is indeed generated setting $P = 5$. Thus, this is our default approach to choosing the best P .

6 Bayesian Angular Inference for ADNI Data

In this section, we implement the Bayesian angular inference scheme to conduct scientific investigations on the ADNI data. We illustrate the results of covariate effects through our proposed tangent-normal decomposition in Section 6.1. In section 6.2, we use the separation angle metric to detect regions of differences. Both approaches generate new insights into the neuro-disease development of Alzheimer’s disease.

6.1 Application 1: Tangent-Normal Decomposition of Covariate Effects

Given our motivating ADNI data, we define the *typical* covariate vector \mathbf{X}_{gT} as $\mathbf{X}_{gT} = [1, X_{gT,gender}, X_{gT,age}, X_{gT,MMSE}, X_{gT,APOE-4}]$, where $X_{gT,gender}$, $X_{gT,age}$, $X_{gT,MMSE}$, and $X_{gT,APOE-4}$ are the values for gender, age, MMSE score, and APOE-4 indicator, respectively. As described before, the values of $X_{gT,age}$ and $X_{gT,MMSE}$ are the sample means of age and MMSE score over all the subjects of the g -th group, respectively. We set $X_{gT,APOE-4} = 0$ (no ϵ -4 variance). We then run separate analyses for the two genders by setting $X_{gT,gender}$ be either 1 (male) or 0 (female). This leads to quantification of gender-specific covariate effects. For space, the main paper only presents the effect of APOE-4 for females, illustrated in Figures 5 and 6. Section A.3 in the supplementary includes the results for both genders and other predictors of interest.

Next, we specify the *hazard* covariate vector $\mathbf{X}_{gH}^{(c')}$ for each covariate to be investigated:

a) If the effect of age is of interest, the *hazard* covariate vector $\mathbf{X}_{gH}^{(age)}$ is $[1, X_{gT,gender}, X_{gH,age}, X_{gT,MMSE}, X_{gT,APOE-4}]$ where $X_{gH,age} = X_{gT,age} + 1$; b) If we aim to investigate the effect of MMSE, the *hazard* covariate vector $\mathbf{X}_{gH}^{(MMSE)}$ is $[1, X_{gT,gender}, X_{gT,age}, X_{gH,MMSE}, X_{gT,APOE-4}]$ where $X_{gH,MMSE} = X_{gT,MMSE} - 1$; c) If we plan to investigate the effect of APOE-4, the *hazard* covariate vector $\mathbf{X}_{gH}^{(APOE-4)}$ is $[1, X_{gT,gender}, X_{gT,age}, X_{gT,MMSE}, X_{gH,APOE-4}]$ where $X_{gH,APOE-4} = 1$.

Our goal here is to understand the physiological disruption of white matter by providing more insightful information about the brain's fiber directions. We thus first visualize 1) the values of $\mathbb{E}[m_{gkj}^{(c')}|\text{data}]$ which quantify the magnitude of the covariate effect for c' ; and secondly, 2) the posterior angular means of the *typical* directions and the *deviation* directions for the voxels where the values of $\mathbb{E}[m_{gkj}^{(c')}|\text{data}]$ are larger than 9-th decile of all

the voxels within the regions of interest. The first visualization helps to map the magnitude of the covariate effects at different voxels; the second visualization allows us to learn the role of the covariate on the fiber directions among the voxels with the largest effect magnitudes.

For space constraints, the main paper only includes the covariate-effect analysis related to APOE-4 due to its well-known clinical importance on cognitive decline (see Figure 5). Figure 5 provides $\mathbb{E}[m_{gkj}^{(\text{APOE-4})}|\text{data}]$ -values for each group to understand the magnitude of the effect of APOE-4. The posterior angular means of *typical* direction and *deviation* direction for the voxels where the values of $\mathbb{E}[m_{gkj}^{(\text{APOE-4})}|\text{data}]$ are larger than 9-th decile of all the voxels within fornix depict the effect of APOE-4 on fiber orientations. In our visualization (see Figure 5), APOE-4 in fornix exhibits a heterogeneous effect on the left and right hemispheres of the brain, and the degree of heterogeneity increases with increasing disease severity. Figure 6 illustrates the pattern of the *deviation* directions (green arrows) to understand how the principal diffusion directions are impacted. The covariate APOE-4 has strong effects on the voxels near the posterior columns of fornix, resulting in large deviations of the *typical* directions. These deviations may be the underlying causes of neurodegeneration. In the future, we will analyze this finding in more detail.

6.2 Application 2: Regions of Differences Characterized by Separation Angle

Here, we investigate the regions of differences across different clinical groups. Separation angles characterize the differences, and the result is given in Section A.4 of the supplementary materials. To better visualize the changes, we only color the voxels having separation angles larger than 5° . In general, when we compare different clinical groups to the healthy controls, the separation angles tend to increase with the increasing severity of the cogni-

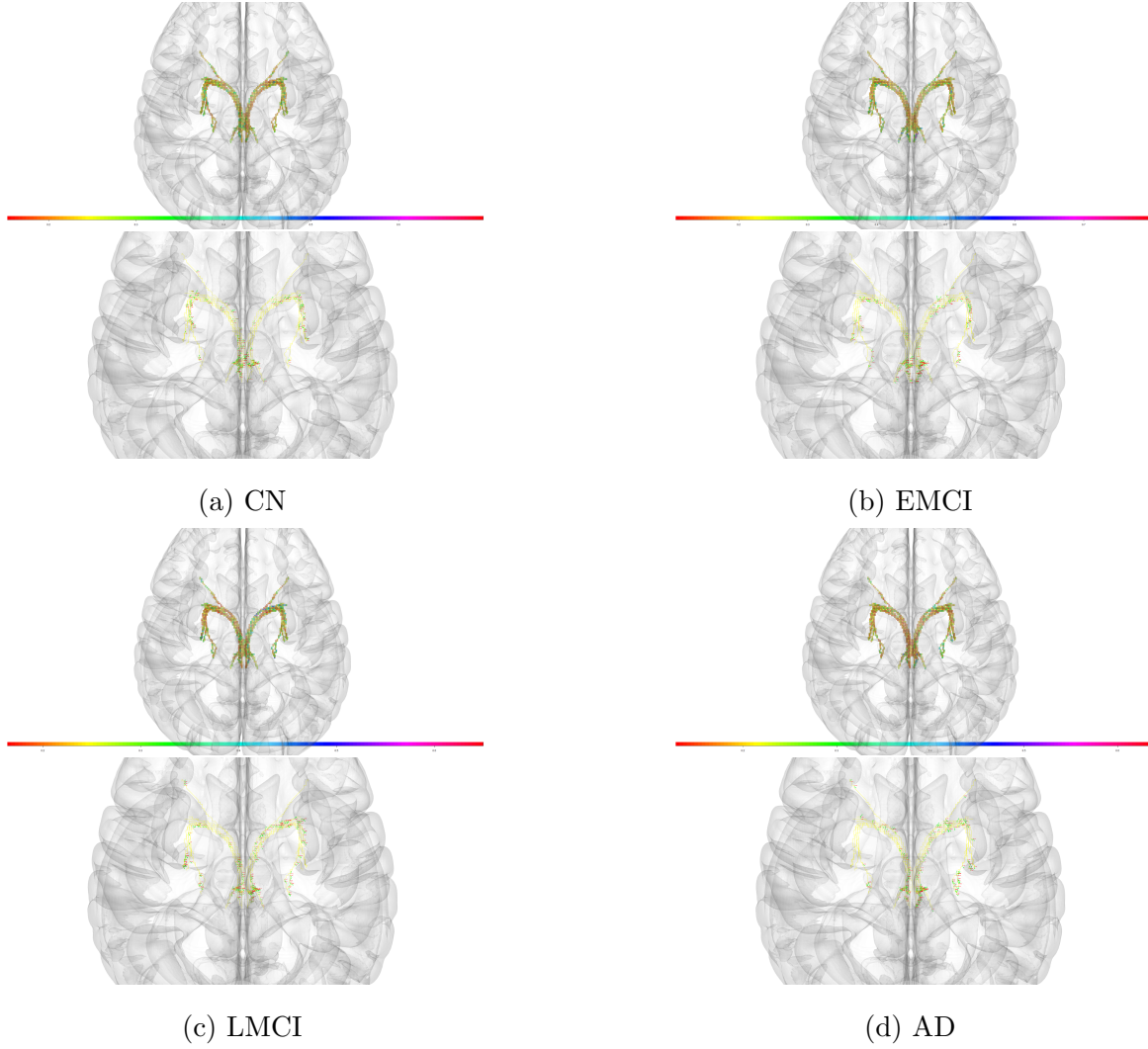


Figure 5: Tangent-normal decomposition of APOE-4 is given. Fornix is the region of interests. For each sub-figure, the upper panel gives $\mathbb{E}[m_{gkj}^{(\text{APOE-4})}|\text{data}]$ which quantifies the *magnitude* of the covariate effect. The color bar below indicates the values; Only for the voxels whose values of $\mathbb{E}[m_{gkj}^{(\text{APOE-4})}|\text{data}]$'s are larger than 9-th decile of all applicable voxels within fornix, we label the red and green arrows. This approach provides a better visualization. The yellow lines connect the voxels which are in the same fiber.

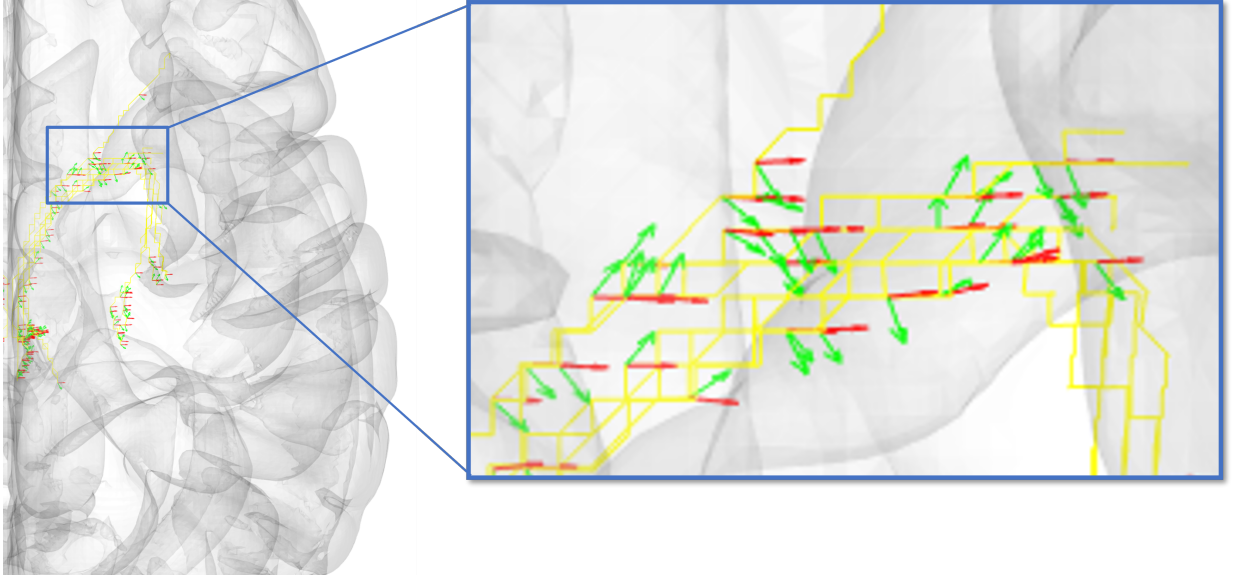


Figure 6: In the left panel, we provide the AD group’s tangent-normal decomposition of APOE-4 effects in the fornix and outline a region in a blue box; In the right panel, we zoom in to get a clear visualization of the region covered by the blue box. The red and green arrows are the posterior angular means of *typical* direction and *deviation* direction, respectively. Only for the voxels whose values of $\mathbb{E}[m_{gkj}^{(\text{APOE-4})}|\text{data}]$ ’s are larger than 9-th decile over all applicable voxels within fornix, we label the red and green arrows. This approach provides a better visualization. The yellow lines connect the voxels which are in the same fiber.

tive impairment. This is a reasonable finding to demonstrate the validity of our proposed method. In the corpus callosum, the anterior-middle regions are apparently different when comparing EMCI-to-LMCI and LMCI-to-AD. Furthermore, the regions of differences are always spatially clustered, demonstrating the importance of inducing spatial dependence in the model.

7 Conclusion and Discussion

This paper develops a novel spatial generalized linear regression framework for modeling principal diffusion directions. Our model is essentially a vMF-distributed error model. The regression model accurately captures the local variation. Given the nature of our fiber tract-based data, the spatial variations are captured using an autoregressive framework. The numerical evaluation of the real data and the synthetic data demonstrates that our proposed method performs overwhelmingly better. Significant scientific findings are obtained by applying our proposed Bayesian angular inference scheme.

Our current analysis is cross-sectional. However, the longitudinal study of ADNI data is becoming more popular recently (Wang and Guo, 2019; Kundu et al., 2019), to identify the underlying mechanisms. The covariate-dependent longitudinal research will be more challenging. For example, the brain images and the other biomarkers are often measured asynchronously (Li et al., 2022). In future work, extending our generalized vMF regression for such asynchronously collected longitudinal data must be an attractive avenue. Furthermore, although we only establish the numerical accuracy of the proposed method, we will also study the theoretical properties in the future.

References

- Aisen, P. S., Petersen, R. C., Donohue, M. C., Gamst, A., Raman, R., Thomas, R. G., Walter, S., Trojanowski, J. Q., Shaw, L. M. and Beckett, L. A. (2010), ‘Clinical core of the Alzheimer’s disease neuroimaging initiative: progress and plans’, Alzheimer’s & Dementia **6**(3), 239–246.
- Barnett, G., Kohn, R. and Sheather, S. (1996), ‘Bayesian estimation of an autoregressive model using markov chain monte carlo’, Journal of Econometrics **74**(2), 237–254.
- Di Paola, M., Spalletta, G. and Caltagirone, C. (2010), ‘In vivo structural neuroanatomy of corpus callosum in Alzheimer’s disease and mild cognitive impairment using different MRI techniques: a review’, Journal of Alzheimer’s disease **20**(1), 67–95.
- Goodlett, C. B., Fletcher, P. T., Gilmore, J. H. and Gerig, G. (2009), ‘Group analysis of dti fiber tract statistics with application to neurodevelopment’, Neuroimage **45**(1), S133–S142.
- Heidelberger, P. and Welch, P. D. (1981), ‘A spectral method for confidence interval generation and run length control in simulations’, Communications of the ACM **24**(4), 233–245.
- Kang, J. and Li, L. (2016), ‘Discussion of “fiber direction estimation in diffusion mri”’, The Annals of Applied Statistics **10**(3), 1162.
- Kundu, S., Lukemire, J., Wang, Y. and Guo, Y. (2019), ‘A novel joint brain network analysis using longitudinal Alzheimer’s disease data’, Scientific reports **9**(1), 1–18.
- Lan, Z., Reich, B. J., Guinness, J., Bandyopadhyay, D., Ma, L. and Moeller, F. G. (2021), ‘Geostatistical modeling of positive definite matrices: An application to diffusion tensor imaging’, Biometrics p. In Press.

- Lee, H. N. and Schwartzman, A. (2017), ‘Inference for eigenvalues and eigenvectors in exponential families of random symmetric matrices’, Journal of Multivariate Analysis **162**, 152–171.
- Li, T., Li, T., Zhu, Z. and Zhu, H. (2022), ‘Regression analysis of asynchronous longitudinal functional and scalar data’, Journal of the American Statistical Association **117**(539), 1228–1242.
- Lindgren, F. and Rue, H. (2015), ‘Bayesian spatial modelling with r-inla’, Journal of statistical software **63**, 1–25.
- Mardia, K. V. (1975), ‘Statistics of directional data’, Journal of the Royal Statistical Society: Series B (Methodological) **37**(3), 349–371.
- Mardia, K. V. (2014), Statistics of directional data, Academic press.
- Mardia, K. V. and Jupp, P. E. (2009), Directional statistics, Vol. 494, John Wiley & Sons.
- Mueller, S. G., Weiner, M. W., Thal, L. J., Petersen, R. C., Jack, C., Jagust, W., Trojanowski, J. Q., Toga, A. W. and Beckett, L. (2005), ‘The Alzheimer’s disease neuroimaging initiative’, Neuroimaging Clinics **15**(4), 869–877.
- Nakata, Y., Sato, N., Abe, O., Shikakura, S., Arima, K., Furuta, N., Uno, M., Hirai, S., Masutani, Y., Ohtomo, K. et al. (2008), ‘Diffusion abnormality in posterior cingulate fiber tracts in alzheimer’s disease: tract-specific analysis’, Radiation medicine **26**(8), 466–473.
- Nowrangi, M. A. and Rosenberg, P. B. (2015), ‘The fornix in mild cognitive impairment and Alzheimer’s disease’, Frontiers in aging neuroscience **7**, 1.

- Oishi, K., Mielke, M. M., Albert, M., Lyketsos, C. G. and Mori, S. (2012), ‘The fornix sign: a potential sign for Alzheimer’s disease based on diffusion tensor imaging’, Journal of Neuroimaging **22**(4), 365–374.
- Podcasy, J. L. and Epperson, C. N. (2022), ‘Considering sex and gender in alzheimer disease and other dementias’, Dialogues in clinical neuroscience .
- Reich, B. J., Guinness, J., Vandekar, S. N., Shinohara, R. T. and Staicu, A.-M. (2018), ‘Fully bayesian spectral methods for imaging data’, Biometrics **74**(2), 645–652.
- Reiman, E. M. and Jagust, W. J. (2012), ‘Brain imaging in the study of alzheimer’s disease’, Neuroimage **61**(2), 505–516.
- Sadigh-Eteghad, S., Talebi, M. and Farhoudi, M. (2012), ‘Association of apolipoprotein e epsilon 4 allele with sporadic late onset Alzheimer’s disease. a meta-analysis’, Neurosciences Journal **17**(4), 321–326.
- Schwartzman, A., Dougherty, R. F. and Taylor, J. E. (2008), ‘False discovery rate analysis of brain diffusion direction maps’, The Annals of Applied Statistics **2**(1), 153.
- Schwartzman, A., Mascarenhas, W. F. and Taylor, J. E. (2008), ‘Inference for eigenvalues and eigenvectors of gaussian symmetric matrices’, The Annals of Statistics **36**(6), 2886–2919.
- Simmons, J. T., Pastakia, B., Chase, T. and Shults, C. (1986), ‘Magnetic resonance imaging in huntington disease.’, American journal of neuroradiology **7**(1), 25–28.
- Soares, J. M., Marques, P., Alves, V. and Sousa, N. (2013), ‘A hitchhiker’s guide to diffusion tensor imaging’, Frontiers in neuroscience **7**.

- Song, H. and Dunson, D. B. (2022), ‘Curved factor analysis with the ellipsoid-gaussian distribution’, arXiv preprint arXiv:2201.08502 .
- Teipel, S. J., Bayer, W., Alexander, G. E., Zebuhr, Y., Teichberg, D., Kulic, L., Schapiro, M. B., Möller, H.-J., Rapoport, S. I. and Hampel, H. (2002), ‘Progression of corpus callosum atrophy in Alzheimer disease’, Archives of Neurology **59**(2), 243–248.
- Wang, Y. and Guo, Y. (2019), ‘A hierarchical independent component analysis model for longitudinal neuroimaging studies’, NeuroImage **189**, 380–400.
- Wong, J. C., Concha, L., Beaulieu, C., Johnston, W., Allen, P. S. and Kalra, S. (2007), ‘Spatial profiling of the corticospinal tract in amyotrophic lateral sclerosis using diffusion tensor imaging’, Journal of Neuroimaging **17**(3), 234–240.
- Wong, R. K., Lee, T. C., Paul, D., Peng, J. and Alzheimer’s Disease Neuroimaging Initiative (2016), ‘Fiber direction estimation, smoothing and tracking in diffusion mri’, The Annals of Applied Statistics **10**(3), 1137–1156.
- Yeh, F.-C., Panesar, S., Fernandes, D., Meola, A., Yoshino, M., Fernandez-Miranda, J. C., Vettel, J. M. and Verstynen, T. (2018), ‘Population-averaged atlas of the macroscale human structural connectome and its network topology’, Neuroimage **178**, 57–68.
- Yuan, Y., Zhu, H., Lin, W. and Marron, J. S. (2012), ‘Local polynomial regression for symmetric positive definite matrices’, Journal of the Royal Statistical Society: Series B (Statistical Methodology) **74**(4), 697–719.
- Zhou, D. (2010), Statistical analysis of diffusion tensor imaging, PhD thesis, University of Nottingham.

Zhu, H., Chen, Y., Ibrahim, J. G., Li, Y., Hall, C. and Lin, W. (2009), ‘Intrinsic regression models for positive-definite matrices with applications to diffusion tensor imaging’, Journal of the American Statistical Association **104**(487), 1203–1212.

Zhu, H., Kong, L., Li, R., Styner, M., Gerig, G., Lin, W. and Gilmore, J. H. (2011), ‘Fadtts: functional analysis of diffusion tensor tract statistics’, NeuroImage **56**(3), 1412–1425.